The Astronomical Journal, 165:90 (17pp), 2023 March https://doi.org/10.3847/1538-3881/acad7e

Investigating Stellar Variability in the Open Cluster Region NGC 381

Jayanand Maurya[1,2,3], Y. C. Joshi[1], A. Panchal[1], and A. S. Gour[2]
[1] Aryabhatta Research Institute of Observational Sciences (ARIES). Nainital, Uttrakhand, India
[2] School of Studies in Physics and Astrophysics, Pt. Ravishankar Shukla University, Raipur, Chattisgarh 492 010, India
[3] Astronomy & Astrophysics Division, Physical Research Laboratory, Ahmedabad, 380009, State of Gujarat, India
Received 2022 April 16; revised 2022 December 14; accepted 2022 December 14; published 2023 February 8

Abstract

We study variable stars in the field of the open cluster NGC 381 using photometric data observed over 27 nights and identify a total of 57 variable stars, six of which are member stars. The variable stars are classified based on their periods, amplitudes, light-curve shapes, and locations in the H-R diagram. We found a rich variety of variable stars in the cluster. We identified a total of 10 eclipsing binaries, of which two are of Algol type while eight are of W UMa type (EW). The estimated ages of these EW binaries are greater than 0.6 Gyr, which is in agreement with the formation time constraint of $\geqslant$0.6 Gyr on short-period eclipsing binaries. The physical parameters of the two EW-type binaries are estimated using PHOEBE model-fitting software. The pulsating variable stars include one each from the δ Scuti and γ Dor variability classes. We determined the pulsation modes of pulsating variables with the help of the FAMIAS package. We obtained 15 rotational variable stars comprising four dwarf stars identified on the basis of their $\log(g)$ versus $\log(T_{\rm eff})$ diagram. These dwarf stars are found to have generally longer periods than the remaining rotational variables.

Unified Astronomy Thesaurus concepts: Open star clusters (1160); Variable stars (1761); Eclipsing binary stars (444); Photometry (1234)

1. Introduction

Open clusters are known to host a rich variety of variable stars (Xue et al. 2019; Joshi et al. 2020a; Sandquist et al. 2020). These stars play a crucial role in our understanding of stars' intrinsic properties such as pulsation, rotation, and emission. In addition to intrinsic properties, extrinsic properties of stars, such as geometrical effects in the case of eclipsing binaries, can also be understood by studying variability. Period–luminosity relations of pulsating stars such as Cepheids and RR Lyrae have been distinctly useful in the study of distance measurement and Galactic structure (Iorio & Belokurov 2019; Skowron et al. 2019; Minniti et al. 2020). Intermediate-age clusters host a large number of δ Scuti stars because their main-sequence (MS) turnoffs lie close to the δ Scuti instability strip. δ Scuti-type variables are main-sequence or subgiant stars of the A3–F0 spectral class that belongs to the lower classical instability strip. Intermediate-age open clusters are the best observing targets for the asteroseismological study of δ Scuti-type stars (Arentoft et al. 2005). γ Dor stars are a relatively new class of main-sequence or subgiant pulsating stars having spectral class A7–F5 and effective temperature $T_{\rm eff}$ between 6700 and 7400 K. These stars are cooler than δ Scuti stars and lie near the red edge of the δ Scuti instability strip.

Eclipsing binary stars are quite common in open clusters as well. They are located above the single-star main sequence in the color–magnitude diagram of the clusters and can be used as a possible distance indicator (Pietrzyński et al. 2019) and in measurements of stellar masses and diameters (Panchal & Joshi 2021). Eclipsing binaries have also been useful in the calibration of theoretical stellar models (Torres et al. 2010). The evolution from eclipsing binaries of Algol type (EA) to W UMa-type binaries (EW) provides an opportunity to understand angular momentum loss, tidal locking, and mass transfer within binary systems (Jiang et al. 2014; Chen et al. 2020; Jiang 2020). Binary systems are also known to contain pulsating companions such as δ Scuti (Liakos & Niarchos 2017; Miszuda et al. 2021). The evolution of a δ Scuti star in a binary system is affected by mass transfer and tidal interaction. The δ Scuti star in a binary system is very useful in theoretical modeling because the physical parameters of binary components can be accurately determined. Some eclipsing binaries exhibit asymmetry in the maxima of the light curves, which is known as the O'Connell effect due to stellar spots on the surface of the components (Joshi et al. 2016).

Photometric variability is also caused by modulation of the brightness due to rotation. Rotational variables belonging to the same cluster population are found to show a period–magnitude relation (Soares-Furtado et al. 2020). These rotational variables have an uneven distribution of the cooler spots on the surface, which produces variation in the magnitude due to the inclination angle of observation. The cooler spots and chromospheric activity generally happen in late-type stars (Long et al. 2021). Drake (2006) found that rotation periods of stars showing chromospheric activity decrease as the distance from the Galactic plane increases. This relation between period and distance from the Galactic plane was attributed to the fact that stars at low altitudes would be more evolved than stars at higher altitudes (Drake 2006). Thus, the study of variable stars provides us with a tool to investigate the state of stellar evolution and the external properties of stars.

In the present study, we carried out a variability search and analysis of the open cluster NGC 381, for which a photometric study was carried out earlier (Maurya & Joshi 2020). This is an intermediate-age sparse open cluster with an estimated age of 447 ± 52 Myr and is located at a distance of 1131 ± 48 pc (Maurya & Joshi 2020). The present variability study has been carried out in an $\sim 18 \times 18$ arcmin^2 region around the cluster

center (R.A. = 01:08:19.57; decl. = +61:35:18.24). This is the very first variability study of cluster NGC 381 and is part of our ongoing project to investigate the variability of poorly studied open clusters (Joshi et al. 2020a). In our previous study, we found a total of 132 member stars of the cluster after applying a 50% probability cutoff in this region. However, Cantat-Gaudin et al. (2018) found a total of 148 member stars belonging to the cluster NGC 381 distributed over a much larger region than that observed in the present study. The present paper is structured as follows. We discuss observations, data reduction, and the transformation of instrumental magnitude to standard magnitude in Section 2. The methods and techniques applied to detect variable stars in the present data set are described in Section 3. We discuss the locations of the variable stars on the H-R diagram and their implications in Section 4. The classification and detailed analysis of the variable stars are discussed in Section 5. We discuss and summarize our analysis in Section 6.

2. Observations and Data Analysis

The observations for the current study were taken using the 1.3 m Devasthal Fast Optical Telescope (DFOT). The DFOT telescope was mounted with a 2k × 2k CCD having a wide coverage of $\sim 18' \times 18'$ over the sky. The data for the variability analysis were collected during 27 nights spanning more than a year starting from 2017 October 1. The observations were accumulated in 738 and 437 frames of the Johnson–Cousins *V* and *I* bands, respectively. We searched for both long- and short-period variables using the collected data. The exposure times varied between 180–220 and 80–120 s for long exposures in the *V* and *I* bands, respectively, whereas short exposures for both bands were in the range of 10–30 s. The observation log for the observations of NGC 381 is given in Table 1.

Table 1
The Log for Observed Time-series Data of the NGC 381 Region

Date	*V* filter Number of frames	*I* filter Number of frames
01/10/2017	9L, 9S	3L, 3S
02/10/2017	36L, 37S	11L, 12S
12/10/2017	28L, 28S	6L, 6S
14/10/2017	4L, 4S	4L, 4S
21/10/2017	3L, 3S	3L, 2S
22/10/2017	32L, 32S	…
23/10/2017	37L, 42S	45L, 44S
29/10/2017	23L, 24S	25L, 25S
30/10/2017	50L, 42S	…
02/11/2017	13L, 15S	8L, 11S
03/11/2017	9L, 10S	10L, 10S
09/11/2017	10L	…
12/11/2017	6L, 6S	17L, 17S
14/11/2017	6L, 6S	7L, 7S
16/11/2017	24L, 21S	26L, 26S
17/11/2017	4L, 4S	…
24/11/2017	8L	…
05/01/2018	19L, 11S	13L, 13S
06/01/2018	17L, 16S	10L, 10S
13/01/2018	3L	3L
22/01/2018	3L	3L, 3S
07/10/2018	10L	3L
20/10/2018	7L	…
01/12/2018	18L	19L
04/12/2018	21L, 12S	12L, 12S
07/12/2018	8L	…
14/01/2019	4L, 4S	5L, 5S

Note. "L" and "S" denote long and short exposures respectively.

The image cleaning procedures such as bias correction, flat-fielding, and removal of cosmic rays were completed using suitable IRAF packages. We used DAOPHOT II packages and processes described by Stetson (1987) to obtain instrumental magnitude through the point-spread function (PSF). The PSF technique is preferred for crowded fields like star clusters. Stars on the edges of some frames can contaminate the magnitudes of adjacent stars and give a false sense of variability. We, therefore, removed all the data points within 20 pixels from the edges of each frame. We used the DAOMATCH and DAOMASTER packages of DAOPHOT II to cross-match the same stars in different frames. The cluster NGC 381 was observed on 2017 October 21 with Landolt's standard field SA 92 for the photometric calibration. The standardized data of NGC 381 were used in its photometric study (Maurya & Joshi 2020). We converted the instrumental magnitude of the stars detected in frames of variability data to the standard magnitude by comparison with the standard data used in Maurya & Joshi (2020). The following conversion formula is used for obtaining the standard magnitudes of stars:

$$V = a_1 \times v + a_2$$

where a_1 and a_2 are conversion coefficients. *V* is the standard magnitude while *v* is the instrumental magnitude of the same star. The conversion coefficients a_1 and a_2 are calculated through least-squares fits for each frame of variability data. We did not use color terms in the conversion formula because the effect of the color terms was found to be very insignificant in the magnitude calibration. The *I*-band data were reduced using the same methods as discussed for the reduction of *V*-band data. However, the cluster was observed mostly in the *V* band. The number of *I*-band frames collected on any specific night was less than 20 for most nights. Due to a larger number of frames and greater coverage, *V*-band data were used for most of the analysis except for the FAMIAS package. We used both *V*- and *I*-band data for mode identification through the FAMIAS package, which requires multiband data. Only *V*-band observations were used in the search for variability. We produced light curves for a total of 5183 stars. All the light curves were inspected for the presence of variability.

3. Identification

We used the Lomb–Scargle algorithm (Lomb 1976; Scargle 1982) to search for a periodic signal in the time-series data. The Lomb–Scargle method searches very efficiently for periodicity in unevenly spaced data. The period corresponding to the frequency of the maximum power in the power spectrum is generally used for phase calculation and phase-folding of the light curves. We checked all the periodic variables by phase-folding the light curves for their periods. We chose only those variables that show good periodic brightness variation throughout the entire phase.

We found a total of 57 periodic variables with periods ranging from 41 minutes to 10.74 days in the NGC 381 region. We verified the periods and the light curves of these periodic variables using the NASA Exoplanet Archive Periodogram

Table 2
Basic Parameters of the Identified Variable Stars

ID	R.A. (J2000) (hh:mm:ss)	Decl. (J2000) (dd:mm:ss)	V (mag)	Period (day)	ΔV (mag)	$T_{\rm eff}$ (K)	$\log(T_{\rm eff}/{\rm K})$	$M_{\rm bol}$	$\log(L/L_{\odot})$	Membership	Type
199	17.38816	61.47656	19.659	0.64170	0.117	6058	3.78234	5.138103	−0.163241	F	Misc
298	17.37635	61.51619	14.970	2.88585	0.274	7156	3.74758	1.067196	1.465122	F	EA
528	17.34962	61.53601	19.578	0.63944	0.240	5866	3.76832	6.143452	−0.565381	F	Misc
535	17.34960	61.46318	18.186	0.88731	0.103	6708	3.82659	3.906007	0.329597	F	Misc
600	17.34102	61.63476	17.804	0.30660	0.071	4873	3.68779	0.307142	1.769143	F	EW
608	17.34195	61.47071	19.597	0.20628	0.104	5649	3.75199	5.342264	−0.244906	F	Rot
610	17.34198	61.44597	18.093	0.88574	0.095	6352	3.80293	3.072912	0.662835	F	Misc
732	17.32448	61.71775	19.529	0.30934	0.259	6642	3.82227	4.805819	−0.030327	F	EW
737	17.32681	61.43044	16.723	5.90783	0.068	7300	3.86335	1.245203	1.393919	F	Misc
749	17.32584	61.44954	16.834	0.85538	0.061	4331	3.62835	7.357904	−1.051162	F	Rot
1155	17.27404	61.67363	18.785	0.30390	0.056	5382	3.73098	5.404430	−0.269772	F	Rot
1173	17.27376	61.50248	16.161	7.97406	0.042	5058	3.70359	0.672518	1.622993	F	Rot
1217	17.26697	61.65434	16.034	1.70109	0.037	6271	3.71063	3.371889	0.543244	F	Rot
1397	17.25031	61.47081	9.858	2.48932	0.265	8059	4.19605	−4.264955	3.597982	F	EA
1399	17.25022	61.43972	14.344	15.60373	0.065	6029	3.76993	4.701243	0.011503	F	Rot
1441	17.24511	61.51020	16.333	2.28997	0.064	5007	3.69958	0.278268	1.780693	F	Misc
1596	17.22836	61.60860	14.118	0.43500	0.022	7158	3.82861	3.137557	0.636977	M	γ Dor
1602	17.22763	61.58761	15.413	1.13352	0.030	6922	3.80548	3.324183	0.562327	F	Misc
1689	17.21949	61.44122	19.499	0.85503	0.120	5739	3.75883	4.550551	0.071779	F	Misc
1785	17.20845	61.56744	17.962	0.47661	0.207	5841	3.76648	3.387451	0.537020	F	EW
1812	17.20693	61.43172	17.971	0.46948	0.080	5075	3.70547	3.594283	0.454287	F	Rot
1935	17.19160	61.43677	14.743	18.86972	0.059	4966	3.71715	5.490398	−0.304159	F	Misc
2018	17.17960	61.61100	20.054	0.38967	0.153	4119	3.61478	7.402637	−1.069055	F	Misc
2058	17.17713	61.43163	18.790	0.46970	0.107	6259	3.79651	3.889816	0.336073	F	Misc
2092	17.17362	61.44512	16.624	0.46971	0.065	6489	3.80542	3.705286	0.409886	F	Misc
2245	17.15525	61.64929	15.623	0.96225	0.023	7869	3.83518	2.063115	1.066754	F	Misc
2302	17.14846	61.71435	13.743	1.46727	0.042	5976	3.77641	4.751433	−0.008573	F	Rot
2458	17.13336	61.67006	19.243	0.27405	0.106	5012	3.69791	6.883659	−0.861464	F	EW
2472	17.13248	61.60869	13.045	1.27248	0.026	7574	4.02109	0.742912	1.594835	M	Misc
2483	17.13197	61.57956	15.163	0.07504	0.037	6731	3.81758	1.983478	1.098609	F	δ Scuti
2597	17.11615	61.71983	19.354	0.76046	0.110	5804	3.76370	4.313651	0.166540	F	Misc
2618	17.11641	61.58124	17.374	0.24802	0.020	4825	3.68353	0.905611	1.529756	F	Rot
2673	17.10656	61.67836	11.645	12.19928	0.042	7956	3.88981	0.749634	1.592147	M	Misc
2699	17.10342	61.68298	19.325	0.30427	0.081	5658	3.75265	5.028546	−0.119419	F	Rot
2999	17.07245	61.51315	15.389	2.93362	0.035	6516	3.79020	4.144697	0.234121	M	Rot
3005	17.07080	61.60435	19.634	0.31405	0.150	4802	3.68145	5.670018	−0.376007	F	EW
3472	17.02022	61.49097	19.207	0.38882	0.126	5653	3.75225	5.138588	−0.163435	F	EW
3535	17.01155	61.57847	17.657	0.32339	0.112	5784	3.70447	5.917628	−0.475051	F	EW
3680	16.99572	61.62203	19.166	0.84519	0.216	7238	3.85964	3.430055	0.519978	F	Misc
3717	16.99284	61.54328	18.603	0.58746	0.089	4873	3.68783	5.478819	−0.299528	F	Rot
3792	16.98570	61.44255	15.835	0.68694	0.049	4795	3.65312	6.642276	−0.764910	F	Rot
4049	16.95194	61.57502	13.343	2.94373	0.024	7988	3.90244	−0.484138	2.085655	F	Misc
4070	16.95224	61.44262	17.795	0.31974	0.046	5273	3.72202	1.591900	1.255240	F	Misc
4243	16.92789	61.53868	17.463	2.13002	0.084	5615	3.77448	4.823012	−0.037205	F	Misc
4281	16.91943	61.67900	18.635	0.24194	0.054	7211	3.85798	3.439219	0.516313	F	Misc
4283	16.92179	61.55971	19.408	0.84517	0.131	6280	3.79796	4.464289	0.106285	F	Misc
4361	16.90875	61.60868	15.017	0.40748	0.024	6392	3.81621	3.751129	0.391548	M	Misc
4405	16.90401	61.55529	16.117	0.76060	0.032	5239	3.83875	2.403936	0.834332	F	Rot
4525	16.88284	61.72299	20.046	0.26657	0.158	4546	3.65762	5.943748	−0.485499	F	Misc
4705	16.86359	61.57545	18.034	0.55897	0.076	5209	3.70465	3.444240	0.514304	F	Misc
4829	16.84602	61.71936	19.438	0.34551	0.114	4409	3.64436	3.735335	0.397866	F	EW
5091	16.81309	61.56333	14.800	0.78344	0.062	6335	3.80175	3.469250	0.504300	M	Misc
5166	16.80137	61.66182	16.948	0.89365	0.065	6170	3.80247	3.381778	0.539289	F	Misc
5199	16.79518	61.70208	18.722	1.13805	0.126	6601	3.81958	3.488482	0.496607	F	Misc
5370	16.77350	61.65828	19.460	1.14294	0.142	5029	3.70151	6.353474	−0.649389	F	Misc
5423	16.77012	61.50882	15.765	0.46019	0.032	4423	3.64572	−0.725947	2.182379	F	Rot
5451	16.76296	61.61349	16.935	1.13334	0.054	10619	4.02610	0.287079	1.777169	F	Misc

Note. The columns denote star ID, R.A., decl., V magnitude, period, amplitude, $T_{\rm eff}$, $\log(T_{\rm eff})$, bolometric magnitude, luminosity, membership, and types of variability. "M" indicates a cluster member while "F" marks a field star.

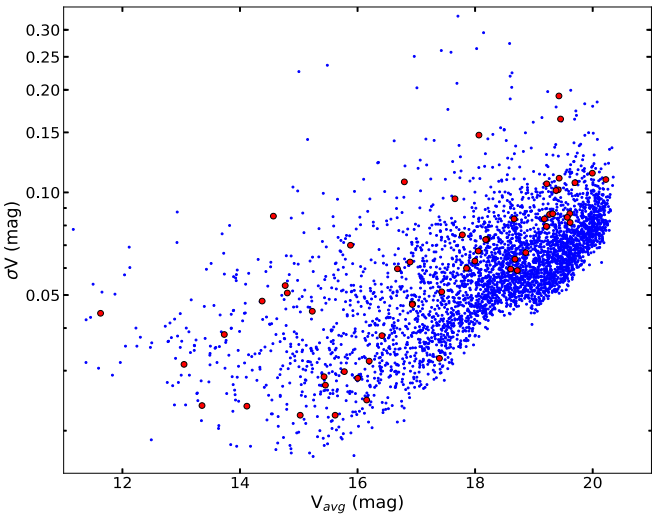

Figure 1. Light-curve RMS as a function of magnitude for the stars in the NGC 381 region. The *y*-axis is on a logarithmic scale. The larger, red points denote variable stars whereas blue points in the background are for nonvariable stars.

service (Akeson et al. 2013) and found that the two periods obtained were generally in agreement. Once the period of a star was known, we determined the phase of each epoch. We generated phase-folded light curves after binning in intervals of generally 0.01 phase. We calculated the mean magnitude for each phase bin. The binned light curves are useful in better identification of variables due to smoothing out of scattered points. We inspected the light curves of all the identified periodic variables for twice the estimated period to find primary and secondary minima.

We investigated the light curves of all the stars detected in the region. These variables were carefully examined for any blending by neighboring stars, and any stars contaminated by light from a neighboring star were discarded. Light curves with periods of $1/n$ day, where n is a positive integer, were excluded from the variability analysis to avoid false variability arising solely due to the aliasing effect. The light curves were plotted after folding the data with phase. We examined the light curves of all the periodic variables for the presence of primary and secondary minima, which is the signature of binary systems, by plotting phase-folded light curves corresponding to twice the obtained periods. The amplitude of the variation in periodic variables was calculated by taking half of the difference in the mean magnitudes of the three faintest and the three brightest points in the curves (Joshi et al. 2020a). We have provided the basic parameters such as period, amplitude, and magnitude in Table 2.

We found a total of 57 periodic variables after all the mentioned examinations. We have determined the light-curve RMS to investigate the spread in data points for variable stars. A plot of the light-curve RMS against the mean magnitudes of the stars is shown in Figure 1. It is evident from the figure that variable stars are generally associated with a larger standard deviation in magnitude than nonvariable stars. The finding chart for all 57 variable stars is given in Figure 2. The obtained periodic variables include 39 short-period ($p < 1$ day) and 18 long-period ($p > 1$ day) variables. The mean magnitudes of these variable stars vary from 9.858 to 20.054 mag in the V band. Their estimated periods are in the range from ∼3 hours to ∼19 days while amplitude variation is between 0.022 and 0.256 mag. We found 10 out of 57 periodic variables to be eclipsing binary stars. The light curves of the variables other than eclipsing binaries and RS CVn stars are shown in Figure 3. Six stars out of these 57 variables are member stars as mentioned in Table 2. The 51 remaining variable stars belong to the field population found in the region of cluster NGC 381.

4. Variable Stars and H-R Diagrams

The H-R diagram basically represents the empirical relation between spectral type and luminosity. Other forms of the H-R diagram can be temperature versus luminosity or color index versus absolute magnitude. The location of a star on the H-R diagram is affected by factors like stellar wind, magnetic field, rotation, and chemical abundance besides initial mass and age. The position of a variable star on the H-R diagram provides us with information about its evolutionary stage. H-R diagrams have also been immensely useful in classifying variable stars because they offer constrained regions for different classes of variable stars.

4.1. Color–Magnitude Diagram

The absolute G versus $(G_{BP} - G_{RP})$ color–magnitude diagram (CMD) has been useful in the classification of variable stars. The CMD is particularly important as it provides constrained regions for variable types such as eclipsing binaries, rotational, eruptive, and cataclysmic variables besides pulsating variables (Gaia Collaboration et al. 2019; Sanghi et al. 2021). Pulsating variables like δ Scuti and γ Dor have very localized clumps on the CMD. The separate locations of variables on the CMD help in removing ambiguity due to the similarity in light curves of two different classes of variables (Sanghi et al. 2021). We used absolute G magnitudes, G_{BP}, and G_{RP}-band data for 35 variables provided by Anders et al. (2019). In the study, the absolute G magnitudes were calculated using precise Gaia DR2 parallaxes. These magnitudes for the variable stars are given in Table 3. We show the CMD constructed from these 35 variable stars in Figure 4.

The CMD for variable stars in the present study indicates the absence of stars like the long-period pulsating variable α Cygni, R Coronae Borealis, V361 Hydrae, and ZZ Ceti stars because constrained regions for these types of stars lie outside the current CMD (Gaia Collaboration et al. 2019). We have considered the position of variable stars on the CMD during their classification.

4.2. H-R Diagram

We examined the $\log(L/L_{\odot})$ versus $\log(T_{\rm eff})$ H-R diagram in the present study to find the evolutionary stage of the identified variable stars. The effective temperature, $T_{\rm eff}$, of 24 stars was available in the catalog provided by Bai et al. (2019). These temperatures were calculated using a large training sample for regression of about four million stars, which makes their estimated effective temperatures more precise than the effective temperatures of Gaia DR2. We used effective temperatures from the catalog of Anders et al. (2019) for an additional 11 stars. $\log(T_{\rm eff})$ for the remaining 22 variable stars was calculated from $(B - V)_0$ color through Torres (2010) relations using distances from Bailer-Jones et al. (2018) and reddening from the 3D reddening map given by Green et al. (2019), which provides reddening $E(g - r)$ with very good resolution for given R.A., decl., and distance. We calculated $E(B - V)$ from $E(g - r)$ using extinction ratio relations given by

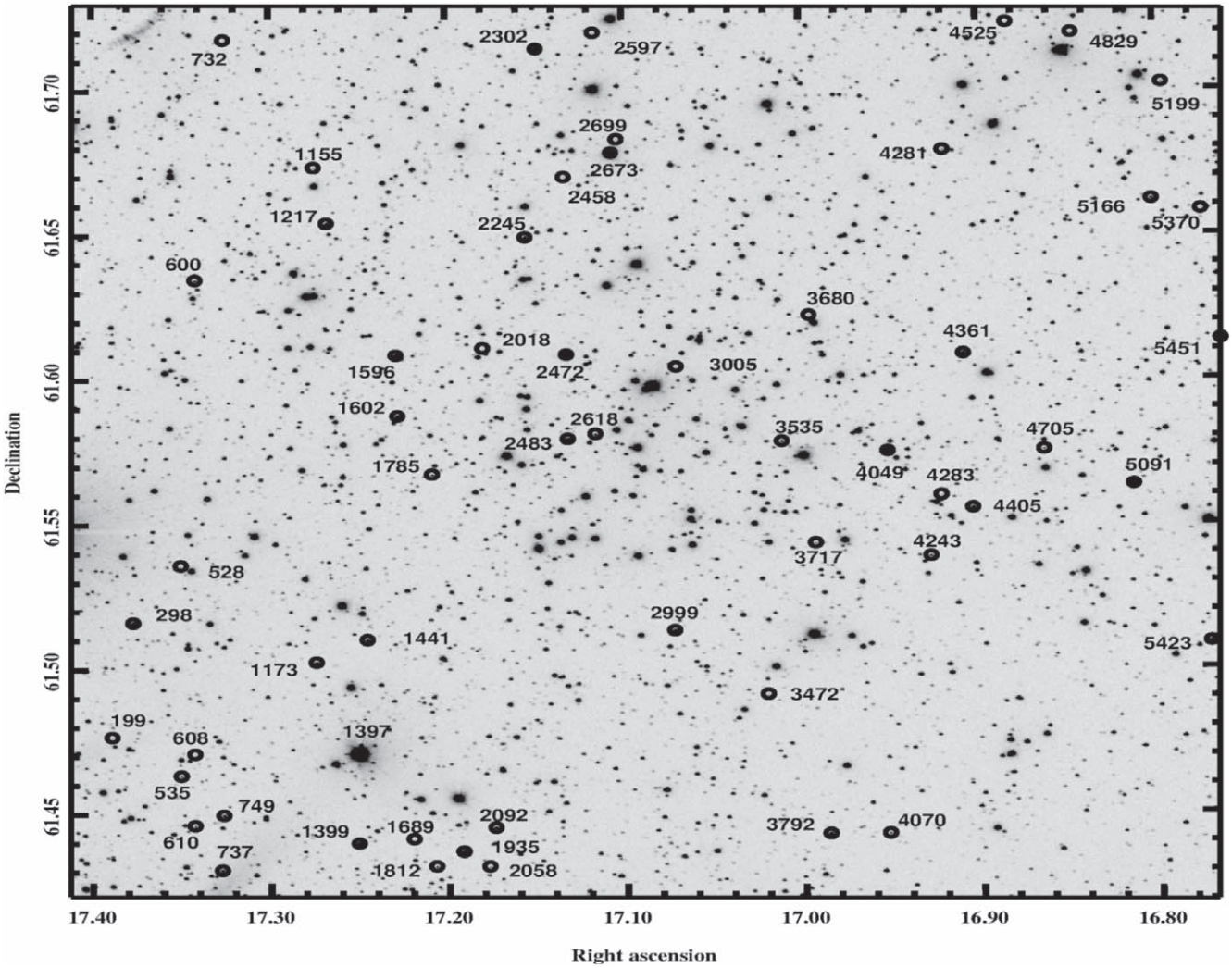

Figure 2. The finding chart for 57 periodic variables detected in the NGC 381 region. Variable stars are marked by circles and labeled with their IDs. The R.A. and decl. are given in degrees.

Wang & Chen (2019). We then calculated $(B-V)_0$ values from the $(B-V)$ color of the star using $E(B-V)$. These values of $\log(T_{\rm eff})$ were used in calculation of logarithmic luminosity, $\log(L/L_{\odot})$, using the method described by Torres (2010). The logarithmic luminosity values were calculated using the following equations:

$$M_{\rm bol} = M_v + {\rm BC}_v$$
$$\log(L/L_{\odot}) = -0.4(M_{\rm bol} - M_{\rm bol_{\odot}}).$$

The bolometric magnitude M_v is calculated from magnitude in the V band, distance, and A_v extinction. The values of distance and extinction were taken from Anders et al. (2019) and were estimated with Gaia DR2 data. The bolometric correction ($\rm BC_v$) values were calculated using empirical relations given by Torres (2010). $M_{\rm bol_{\odot}}$ in the above equations is the bolometric magnitude of the Sun, which is taken as 4.73 mag (Torres 2010). Once we had calculated $\log(T_{\rm eff})$, the values of $\log(L/L_{\odot})$ were calculated using the above described relations through Torres' (2010) method of $\rm BC_v$ calculation. We plotted the H-R diagram using the calculated $\log(T_{\rm eff})$ and $\log(L/L_{\odot})$ as shown in Figure 5. The instability strips corresponding to δ Scuti, γ Dor, slowly pulsating B-type (SPB), and Cepheid stars are also marked in the H-R diagram.

The instability strips belonging to high-mass stars like SPB stars do not host any star in the H-R diagram of NGC 381. As most of the variable stars in the NGC 381 region belong to the field population, the lack of high-mass variable stars is consistent with the expectations. We found three variable stars in the gap between SPB and δ Scuti strips, which is theoretically inhibited for pulsation. The variable stars in this gap have also been found in previous studies (Balona et al. 2011; Joshi et al. 2020b) and we discuss this phenomenon in Section 5. There are few low-mass variable stars like δ Scuti and γ Dor in the instability strips. The locations of variable stars in the H-R diagram as well as CMD have been used for the classification of variables. In the following section, we describe the individual characteristics of the different classes of variables found in our study.

5. Classification

The classification of variable stars is necessary for their comparative study. The variable stars have been classified based on period, amplitude, effective temperature, mass, the shape of the light curves, and location on the H-R diagram.

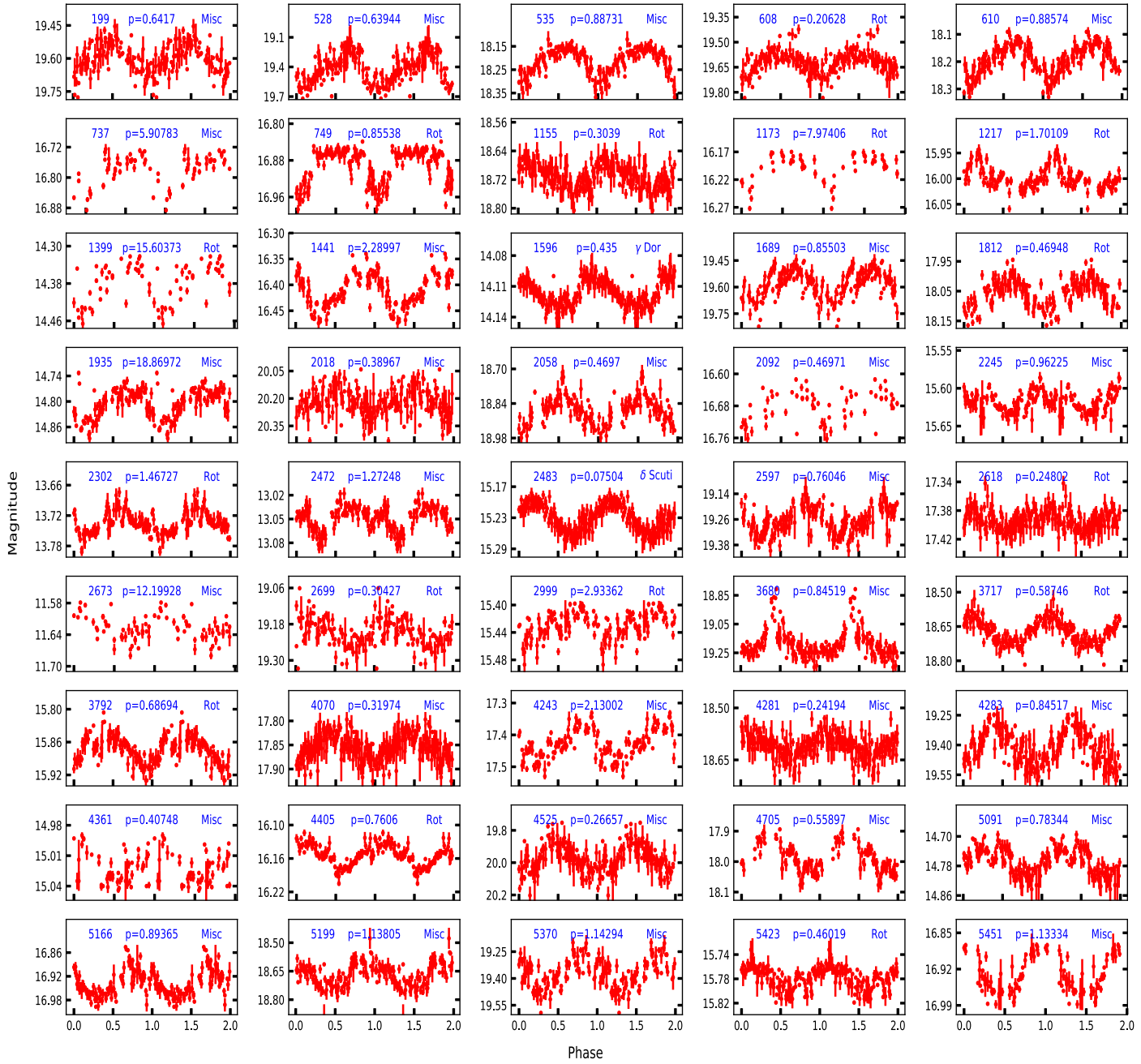

Figure 3. Phase-folded light curves of periodic variable stars identified in the NGC 381 region. The plots are given for twice the phase value for a good presentation. The star IDs, periods (p) in days, and variability types are noted at the top of each light curve. The original light curves and Lomb–Scargle periodograms are shown in Figure 14 in the Appendix. The light curves for the eclipsing binaries are given in Figure 6. The light curves for stars 1602 and 4049 are shown in Figure 12. These two stars are reported to be RS Canum Venaticorum-type (RS CVn) variables in the literature (Watson et al. 2006).

Pulsating variable stars are known to be located in various instability strips on the H-R diagram related to the pulsation mechanism. Additionally, the locations of the variable stars on the CMD diagram were also considered for determining the variability class. Despite our best efforts, we acknowledge that there can be some ambiguity in the classifications of variable stars; for instance, a rotational variable can also show primary and secondary minima. Similarly, there can be ambiguity in the classification of δ Scuti and γ Dor stars because they belong to nearby instability strips on the H-R diagram. Gaps in the data can also affect the shape of the light curves, especially for low-amplitude variables.

5.1. Variability Caused by Eclipses and Rotation

5.1.1. Eclipsing Binaries

Eclipsing binaries have been very useful in the precise determination of masses, luminosities, radii, and distances (Pietrzyński et al. 2019; Stassun & Torres 2021). We identified a number of eclipsing binaries from inspection of their light curves. Photometric eclipsing binaries are identified through specific features such as the size of the primary and secondary minima in the light curves. These specific features can be theoretically explained by Roche lobe geometry. In an eclipsing binary of Algol type (EA), one of the component

Table 3
G, G_{BP}, and G_{RP} Magnitudes Taken from Gaia eDR3 mag

ID	G (mag)	G_{BP} (mag)	G_{RP} (mag)	$G_{BP} - G_{RP}$ (mag)	G_0
298	14.3877	14.7998	13.7793	1.020500	0.666100
600	17.5191	18.0799	16.8012	1.278700	0.488836
610	17.7972	18.4208	17.0336	1.387200	3.048655
737	16.5466	17.0495	15.8812	1.168300	1.267372
749	16.1014	17.1122	15.1064	2.005800	7.622625
1173	15.6201	16.4421	14.7247	1.717400	0.709279
1217	15.7076	16.2976	14.9249	1.372700	3.387695
1397	9.8681	10.002	9.6066	0.395400	−2.927836
1399	14.1543	14.5896	13.5438	1.045800	4.637926
1441	15.8335	16.6254	14.955	1.670400	0.321563
1596	13.9532	14.3141	13.4158	0.898300	3.036791
1602	15.2371	15.6453	14.6385	1.006800	3.246058
1785	17.6741	18.3018	16.8906	1.411200	3.367079
1812	17.5073	18.2624	16.6488	1.613600	3.587901
1935	14.4212	15.0251	13.6831	1.342000	5.468198
2092	16.4239	16.8871	15.7813	1.105800	3.641529
2245	15.5027	15.7892	15.0404	0.748800	1.96228
2302	13.9527	13.9487	12.8531	1.095600	4.802494
2472	12.9203	13.2031	12.4731	0.730000	0.992314
2483	14.9365	15.416	14.2758	1.140200	1.914954
2618	16.7424	17.5992	15.8243	1.774900	0.91183
2673	11.5709	11.7849	11.2164	0.568500	0.711613
2999	15.1195	15.5919	14.4665	1.125400	4.026561
3535	17.0551	17.7956	16.2115	1.584100	5.800122
3792	15.3578	16.0753	14.5375	1.537800	6.807869
4049	13.2593	13.4677	12.8803	0.587400	−0.627663
4070	17.3223	18.103	16.4568	1.646200	1.619608
4243	16.9251	17.6806	16.0811	1.599500	4.692011
4361	14.7457	15.2224	14.0984	1.124000	3.604831
4405	15.5044	16.3757	14.5575	1.818200	2.561388
4705	17.3425	18.225	16.4173	1.807700	3.404837
5091	14.7421	15.1451	13.9861	1.159000	3.56836
5166	16.5781	17.1719	15.8359	1.336000	3.255291
5423	14.9632	16.0395	13.9387	2.100800	−0.506022
5451	16.661	17.1892	15.9542	1.235000	0.634745

Note. The absolute G magnitudes denoted by G_0 are used from Anders et al. (2019). The first column gives star IDs.

stars has filled or overflowed its Roche lobe. The light curves of these variables are identified by the clear beginning and end of the maxima and minima. The light curves of eclipsing binaries of β Lyrae type (EB) do not show any definite start or end of eclipses as light varies continuously. EBs are semidetached systems that have gravitationally distorted components and hence have continuously varying light curves. W Ursae Majoris-type (EW) eclipsing binaries, or W UMa stars, are marked by almost equal primary and secondary minima in the light curves. EW binaries are contact binaries consisting of ellipsoidal components with periods generally less than 1 day and no clear onset or end of the eclipses. It has been found that EA binaries evolve to EW through angular momentum loss and mass transfer (Qian et al. 2018).

We found two EA and eight EW binaries in the NGC 381 region. The high number of EW binaries in this region compared to EA binaries is consistent with the fact that a study by Chen et al. (2020) detected many times more EW binaries than EA binaries. The light curves for obtained eclipsing binaries are given in Figure 6. The light curves of binary stars 298 and 1397 are marked with a clear beginning and end of primary and secondary minima. The binary star ID 1397 is located on the CMD in the region mostly occupied by EA-type binaries (e.g., Gaia Collaboration et al. 2019). Therefore we classified star 1397 as an EA-type eclipsing binary. The light-curve properties of binary star 298 suggest it to be an EA-type eclipsing binary, which is also supported by its location on the CMD. The light curves of the remaining eight eclipsing binaries, having IDs 600, 732, 1785, 2458, 3005, 3472, 3535, and 4829, show characteristics of EW-type binaries. The stars having IDs 600, 1785, and 3535 are also shown on the CMD and their locations are consistent with their classification as EW stars. The positions of the EA binary stars 298 and 1397 on the CMD are significantly higher than the locations of EW binary systems, indicating primary stars in the case of EA binaries are of earlier spectral type than primary stars of EW systems. We found the periods of EW-type binaries to be significantly shorter than those of EA-type binaries, as expected by theories of evolution from EA to EW (Chen et al. 2020). The periods of all these binaries are found to be longer than the observed period cutoff of 0.23 days for eclipsing binaries (Rucinski 2007; Norton et al. 2011). This sharp period cutoff is considered to be related to the nuclear evolution timescale of the primary component (Chen et al. 2020).

5.1.2. Physical Parameters of Eclipsing Binaries

Through Empirical Relations

It was found that the absolute parameters of an eclipsing binary depend on the period and the mass ratio of the system (Latković et al. 2021). We calculated the physical parameters of EW stars using the empirical relations of Latković et al. (2021) given as follows (where mass, radius, and luminosity are given in solar units):

$$M_1 = (2.94 \pm 0.21)P + (0.16 \pm 0.08)$$
$$M_2 = (0.15 \pm 0.17)P + (0.32 \pm 0.06)$$
$$R_1 = (3.62 \pm 0.13)P + (0.04 \pm 0.05)$$
$$R_2 = (1.56 \pm 0.13)P + (0.16 \pm 0.05)$$
$$L_1 = (13.98 \pm 0.75)P + (3.04 \pm 0.27)$$
$$L_2 = (3.66 \pm 0.26)P + (0.69 \pm 0.09).$$

We also calculated the ages of these EW stars using the method described in Yildiz & Doğan (2013) and used by Latković et al. (2021). The secondary components of EW-type binaries are currently less massive than the primary stars. However, the secondary stars are found to be more luminous than the luminosity expected for the current mass. This extra luminosity is interpreted as a hint of its mass before mass transfer. M_L is defined as the mass of an isolated star with luminosity equivalent to the luminosity of the secondary star. The quantity $\delta M = M_L - M_2$ is used to find the initial mass of the secondary star, M_{2i}. The values of M_L and M_{2i} are calculated as follows:

$$M_L = \left(\frac{L_2}{1.49}\right)^{0.237}$$
$$M_{2i} = M_2 + 2.5(\delta M - 0.07)^{0.64}.$$

The initial mass ratio can be calculated in the following form:

$$\frac{1}{q_i} = \frac{M_1 - (M_{2i} - M_2)(1 - \gamma)}{M_{2i}}$$

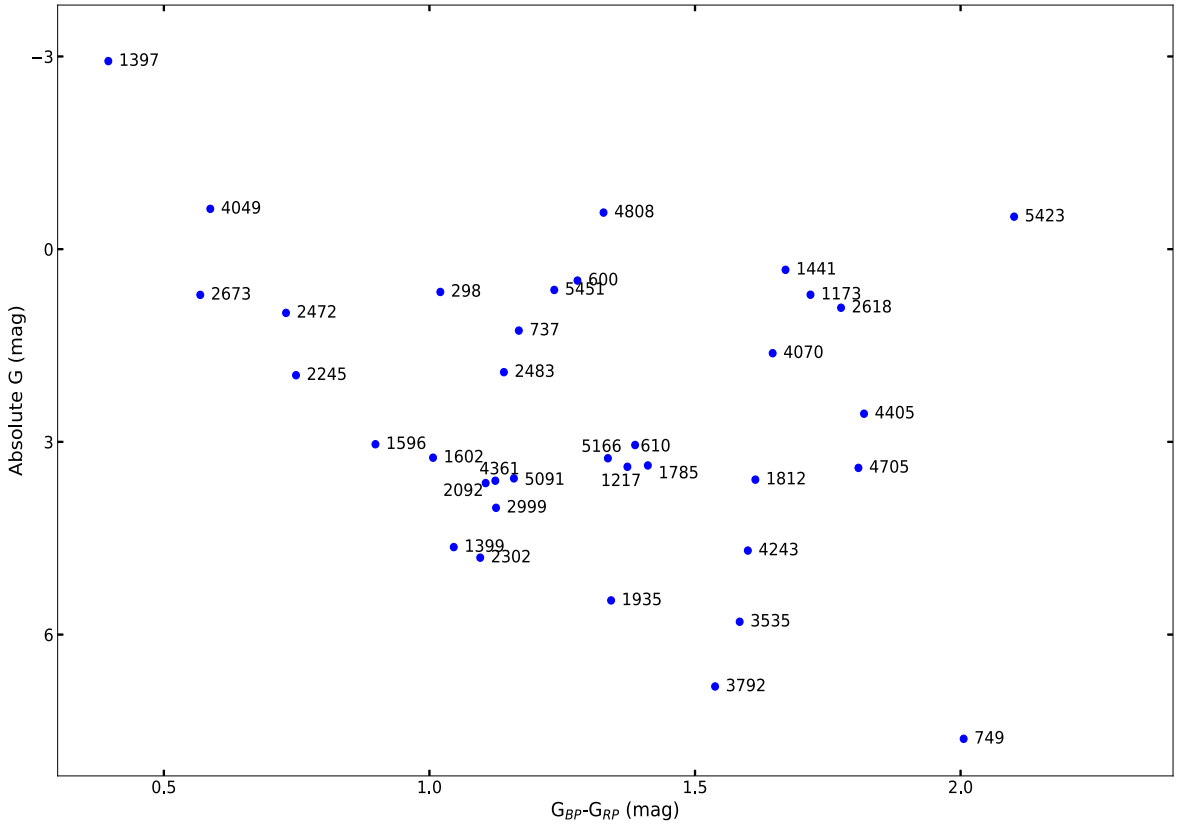

Figure 4. Plot of absolute G vs. ($G_{\rm BP} - G_{\rm RP}$) color–magnitude diagram for the 35 variable stars identified in the NGC 381 region.

where γ is the ratio of the mass loss from the system to the value of ($M_{2i} - M_2$), which we considered as 0.664 for these calculations (Latković et al. 2021). The value of mass ratio was found to vary with mass difference δM for EW-type eclipsing binaries while there was no correlation for EA-type eclipsing binaries (Yildiz & Doğan 2013). The correction was applied for mass difference $\delta M < 0.35$ (refer to Figure 7 of Yildiz & Doğan 2013) for EW stars. We calculated δM and found that all the EW stars found in our study have $\delta M > 0.35$, so we did not use the corrections. We employed the following relation to calculate the ages of binary components:

$$t_{\rm MS} = \frac{10}{M^{4.05}}[0.0056(M + 3.993)^{3.16} + 0.042]$$

where M is the mass of the component whose age is to be determined. The age of the binary system itself for an EW-type star is calculated as age $= t_{\rm MS}(M_{2i})$, i.e., by putting $M = M_{2i}$ in the above equation. However, if the age of the binary system calculated by this method is greater than the age of the primary star then the latter should be taken as the age of the binary star system (Latković et al. 2021).

The primary temperature of EW systems has been found to be correlated with the orbital period (Jayasinghe et al. 2020a; Latković et al. 2021). We calculated the primary temperatures of EW stars having periods of less than 0.5 days using the following relation given by Latković et al. (2021):

$$T_1 = -(2752 \pm 320) \times P + (6745 \pm 100)$$

where T_1 is the temperature of the primary (in kelvin) and P is the orbital period of the EW binary. The values of the physical parameters calculated using the empirical relations are given in Table 4. We caution about the reliability of the obtained parameters corresponding to the star with ID 600 because parameters of EW stars with periods greater than 0.5 days have hardly been reliable (Latković et al. 2021). The ages of the remaining stars are found to be greater than 0.6 Gyr, which is consistent with the formation time constraint of $\geqslant$0.6 Gyr for short-period binaries (Hwang & Zakamska 2020). The obtained temperature of the primary component corresponds to the spectral class G. These temperature values are consistent with the classification of these stars as EW binaries because the spectral classes of both the components of an EW system are generally found to be later than F class.

Through Model Fitting

Eclipsing binaries vary in brightness with time due to their orbital geometry and alignment from the observer's point of view. We can determine many physical parameters and properties such as period, mass, distance, and radii accurately utilizing photometric and spectroscopic methods. The unique features of the evolution and formation of eclipsing binaries can be studied via continuous monitoring. In our work, we identified 10 eclipsing binaries including eight of EW type. The V-band photometric light curves of two of these eight EWs are analyzed with the help of the PHOEBE software package. The rest of the identified eclipsing binaries require more photometric observations as some parts of their light curves are missing.

PHOEBE is one of the most popular tools used for modeling the light curves and radial velocity (RV) curves of eclipsing

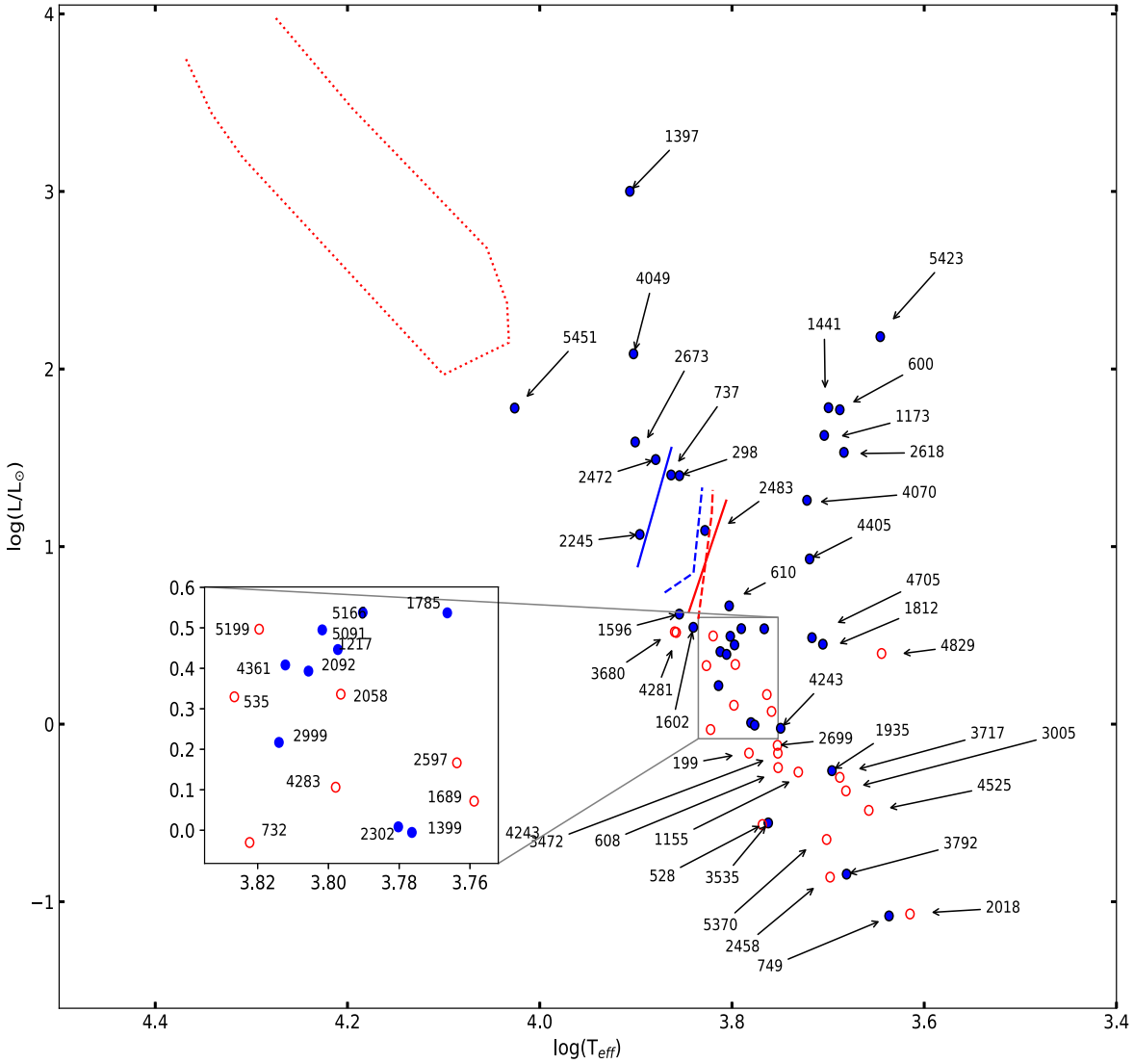

Figure 5. H-R diagram of variable stars found in the NGC 381 region. The instability strips corresponding to slowly pulsating B-type, δ Scuti, and γ Dor stars are shown by red dotted curve, continuous line, and dashed line, respectively. The blue filled points denote the stars that were available in the catalogs of Anders et al. (2019) and Bai et al. (2019). The open circles represent stars whose effective temperatures were calculated using Torres' (2010) relations.

binaries. It is based on the Wilson–Devinney code, which is written in FORTRAN. We used PHOEBE 1.0, which provides a GUI and scripter tool for modeling eclipsing binaries. As the two binaries 0732 and 1785 are reported as EWs, we selected an overcontact binary not in thermal contact as the fitting model in PHOEBE. The temperature of the systems is determined using the color–temperature relation provided by Torres et al. (2010). The estimated $T_{\rm eff}$ is used as the temperature of the primary component. The calculation of mass ratio ($q = m_2/m_1$) is the first step in modeling the photometric light curve. An accurate determination of q requires an RV observation, but in its absence, photometric light curves can also be used to constrain the q parameter around its real value. It has been observed that the photometric mass ratio is reliable for total eclipsing binaries only (Hambálek & Pribulla 2013). So, as the inclination angle decreases, the uncertainty in the photometric mass ratio increases. But due to the absence of RV data, we are dependent only on the q-search method. In this method, some known parameters such as the time of minimum, period, $T_{\rm eff}$ of the primary, surface albedo, and gravity brightening are fixed. The other quantities such as inclination (i), $T_{\rm eff}$ of the secondary, surface potential (Ω), and luminosity (l_1 and l_2) are set as free parameters. q is varied in small steps, and corresponding to each q a best-fit model is obtained with the number of iterations. The cost function corresponding to the best-fit model for each q is noted. The value of q that corresponds to the minimum cost function is assumed as the actual mass ratio. The process of q-search is repeated for both of the binary systems and the estimated values of q for 0732 and 1785 are 0.42 and 0.26, respectively. The PHOEBE scripter was run multiple times with these q parameters to get the final solution. The fitted light curves are plotted with the observed data in Figure 7.

Both systems 0732 and 1785 show a small difference in the levels of primary and secondary minima, so some temperature difference between the two components can be expected. The final model shows temperature differences of almost 500 and 150 for the binaries 0732 and 1785, respectively. The fill-out factor is found to be 0.31 for 0732 and 0.53 for 1785. The mass and radii of the primary component are determined using the relations of Gazeas (2009). The parameters determined from our observations using PHOEBE and these relations are given

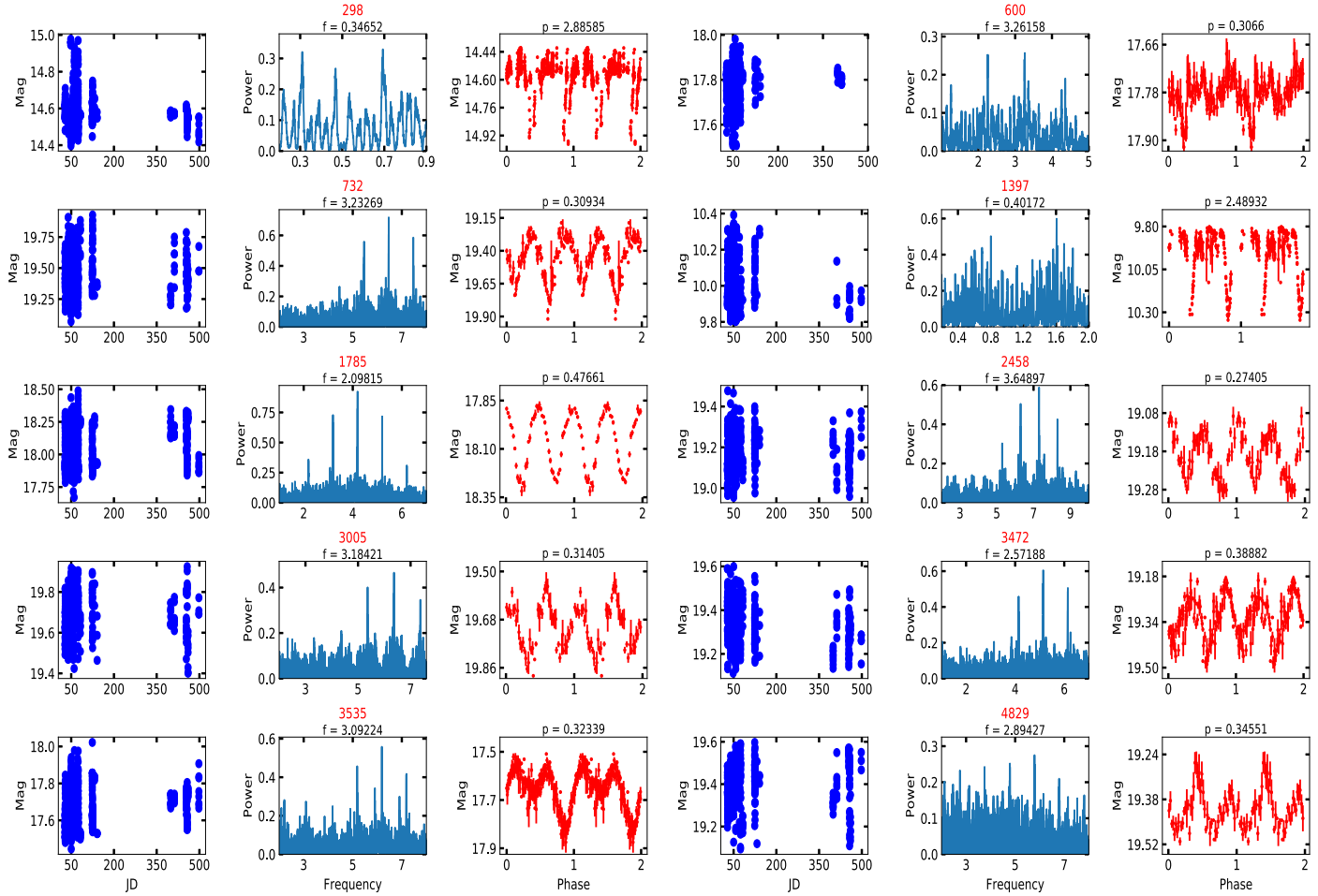

Figure 6. The original light curves (left subplot), Lomb–Scargle periodograms (middle subplot), and phase-folded light curves (right subplot) of each eclipsing binary star found in the NGC 381 region. The periods (p) and corresponding frequencies (f) are also shown in the subplots. Star IDs are given at the top of each plot.

Table 4
Calculated Parameters of Eclipsing Binaries Using Empirical Relations

ID	M_1 ($M_\odot$)	M_2 ($M_\odot$)	R_1 ($R_\odot$)	R_2 ($R_\odot$)	L_1 ($L_\odot$)	L_2 ($L_\odot$)	Age (Gyr)	T_1
600	1.963	0.412	2.260	1.117	11.613	2.934	0.589	⋯
732	1.069	0.366	1.160	0.643	7.365	1.822	0.755	5894
1785	1.561	0.391	1.765	0.904	9.703	2.434	0.647	5433
2458	0.966	0.361	1.032	0.588	6.871	1.693	0.786	5991
3005	1.083	0.367	1.177	0.650	7.430	1.839	0.751	5881
3472	1.303	0.378	1.448	0.767	8.476	2.113	0.697	5675
3535	1.111	0.369	1.211	0.664	7.561	1.874	0.744	5855
4829	1.176	0.372	1.291	0.699	7.870	1.955	0.727	5794

Note. M, R, L, and T denote mass, radius, luminosity, and temperature. The subscript 1 denotes the primary star and 2 the secondary.

in Table 5. The system 1785 was also observed by the Zwicky Transient Facility (ZTF, Bellm et al. 2019) survey from 2018 May 18 to 2022 May 31 in *zi*, *zr*, and *zg* bands. Most of the photometric observations are in the *zr* band (1173 data points). To compare the modeling results from our observed data for system 1785, we analyze ZTF *zr*-band data for 1785 with PHOEBE. The *catflags* flag in the ZTF catalog informs the user about the quality of data.[4] The photometric observations corresponding to *catflags* = 0 are used for the modeling. For the ZTF data of system 1785, the q-search method estimated the q value to be 0.24 (±0.03). The secondary temperature and inclination for system 1785 are determined as 4965 (±135) K and 71° (±2°), respectively, using the ZTF data. Thus, the modeling results from ZTF data are similar to the results obtained from our observed data. All the results are determined using the photometric mass ratio and *V*-band photometric data. For the modeling, binned light curves are used and there is also some scattering in data points. These results can be considered as preliminary; more accurate results will require multiband photometry of these systems. The use of long-term multiband photometric data can also help in the analysis of other long-term effects such as period variation, surface activity, etc.

[4] https://irsa.ipac.caltech.edu/onlinehelp/ztf/help.pdf

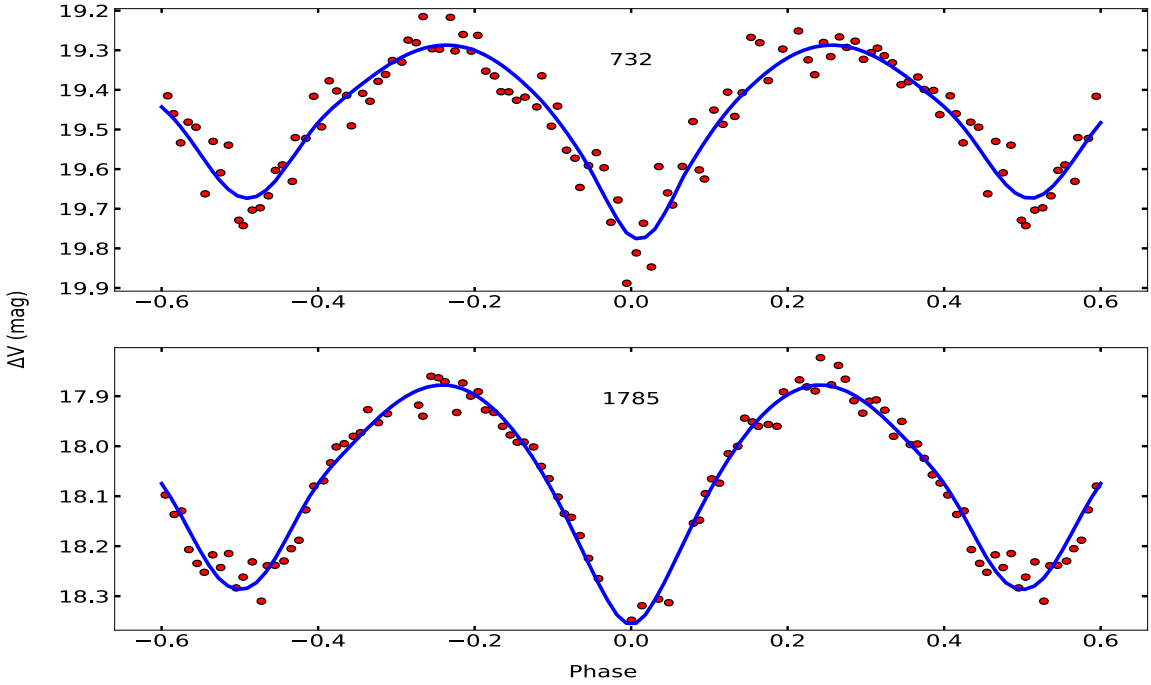

Figure 7. The light curves of the two EW binary systems whose physical parameters are estimated using PHOEBE code model fittings. The blue continuous curves show the best model fits of the PHOEBE model fitting code. The ID for each binary system is given at the top of each subplot.

Table 5
Physical Parameters Estimated by PHOEBE Model Fitting of the Light Curves of the EW Binary Systems ID 0732 and ID 1785

Parameters	ID 0732	ID 1785
Period (days)	0.30935	0.47661
q	0.42 ± 0.03	0.26 ± 0.05
i (deg)	71 ± 1	72 ± 5
T_1 (K)	6642	5179
T_2 (K)	6116 ± 154	5003 ± 55
Ω_1	2.64 ± 0.03	2.29 ± 0.02
Ω_2	Ω_1	Ω_1
$L_1/(L_1 + L_2)$	0.752	0.794
M_1 ($M_\odot$)	1.06	1.51
M_2 ($M_\odot$)	0.44	0.39
R_1 ($R_\odot$)	1.03	1.65
R_2 ($R_\odot$)	0.71	0.92

5.2. Rotational Variables

Stars showing variability caused by axial rotation of a surface of nonuniform brightness are known as rotational variables. The variation in the surface brightness may be due to the presence of spots and other magnetic activity. The rate of rotation of the surface of a star decreases with increasing age, and this property is used as an age indicator for individual stars (Barnes 2007). Late-type stars (G or K type) with true color $(B-V)_0$ values larger than 0.5 mag (Mamajek & Hillenbrand 2008) are classified as rotational variables. In our study, we found a total of 15 rotational variables having IDs 608, 749, 1155, 1173, 1217, 1399, 1812, 2302, 2618, 2699, 2999, 3717, 3792, 4405, and 5423. The locations of these 15 stars on the CMD were compatible with their classification as rotational variables.

The rotational variable star 2999 is also a member star, which gives us the opportunity to utilize the period–age relations known to apply for rotational variables. We used empirical period–age relations given by Angus et al. (2019) to calculate the period for the star 2999. The $G_{BP} - G_{RP}$ value for the star was found to be 1.1254 mag as given in Table 3. We took the age of the cluster to be 447 ± 52 Myr as previously determined by us (Maurya & Joshi 2020). Using the period–age relation, the period of the rotational variable 2999 was predicted to be 8.8450 days, which is much longer than the value of 2.93362 days determined in the present study.

The locations of stars 2618 and 5423 on the CMD are in the region populated by only rotational ellipsoidal variables. This indicates that these two stars can be classified as rotational ellipsoidal-type variables, which are close binaries exhibiting variability without eclipses due to distortion of orbital motion by the companion star. These variables are known to have generally smaller amplitude than contact binaries (Drake et al. 2017), which is also the case with stars 2618 and 5423. Stars 1173 and 1812 are located in the region of the CMD occupied by rotational ellipsoid variables and RS CVn variables. These two stars did not show distortion of the eclipses in light curves generated from current data to ascertain their classification as RS CVn stars.

We show the distributions of the rotational variables in a $\log(g)$ versus $\log(T_{\rm eff})$ diagram in Figure 8. We notice that the four stars with IDs 1217, 1399, 2302, and 2999 are separated from the others in this plot. These four stars satisfy the criteria for dwarf stars given by Ciardi et al. (2011). Magnetic braking causes a decline in the rotation rates of stars with increasing age (Skumanich 1972). Dwarf stars having spectral class later than F have been found to be long-period variables generally with a period of the order of weeks rather than the shorter period of early-type dwarfs (Ciardi et al. 2011). The dwarf stars 1217, 1399, 2302, and 2999 also have comparatively longer periods than other rotating variables because the effective temperatures given in Table 2 indicate that these stars are of spectral class G. The star 2618 has a mass of 1.36 $M_\odot$ (Anders et al. 2019) and the shortest period of 0.248 days in our list of identified rotational variables. An important transition occurs around 1.3

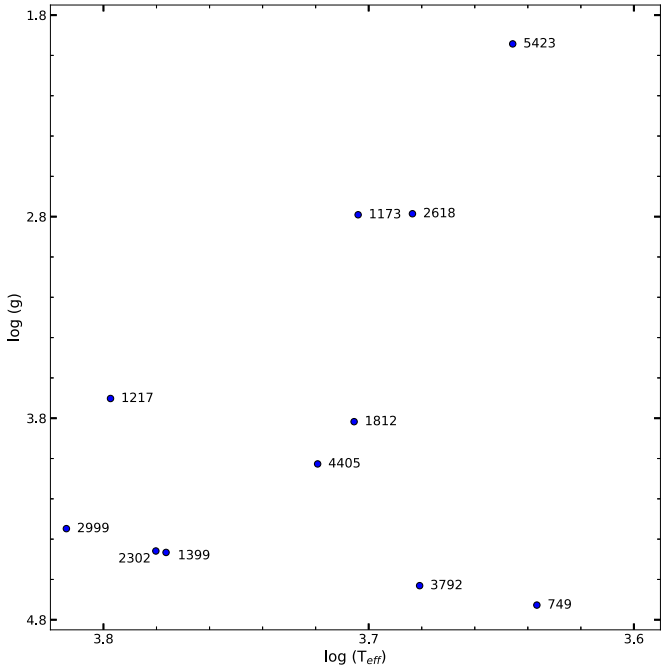

Figure 8. Plot of log(g) vs. log($T_{\rm eff}$) for rotational variables whose log(g) and $T_{\rm eff}$ values are available in the catalogs of Anders et al. (2019) and Bai et al. (2019).

$M_{\odot}$: stars of greater mass than this are generally fast-rotating. In these stars, convective envelopes become so thin that they become unable to produce strong magnetic braking through magnetic winds (van Saders & Pinsonneault 2013).

5.3. Variability Caused by Pulsations

5.3.1. δ Scuti Stars

δ Scuti stars are short-period pulsating variables found in the theoretical instability strip of δ Scuti stars on the H-R diagram. These variables have periods less than 0.3 days and amplitude of the order of a few tenths of a magnitude. δ Scuti stars are of A0–F5 spectral type and lie on the main sequence or the post-main-sequence stages of the H-R diagram (Breger 2000) driven by the κ mechanism of pulsation. δ Scuti stars have intermediate mass (1.5–2.5 $M_{\odot}$; Bedding et al. 2020) with effective temperature in the range 6300–8600 K (Uytterhoeven et al. 2011). Star 2483 is located in the δ Scuti instability strip of the H-R diagram for NGC 381. This star exhibits properties of δ Scuti for a period of 0.07504 days while it also shows the light curve of the binary system for a period of 0.25379 days. The power spectrum of 2483 is shown in Figure 9 whereas the light curve for the period of 0.25379 days is shown in Figure 10. The amplitude corresponding to the period of 0.07504 days was found to be 0.037 mag, as also listed in Table 2. The effective temperature and mass of this star are reported to be 6731 K and 1.696 $M_{\odot}$, respectively (Anders et al. 2019; Bai et al. 2019). On the basis of its period, amplitude, and location on the H-R diagram star 2483 can be classified as a δ Scuti variable star. This star is located within the region assigned for δ Scuti stars on the CMD (Sanghi et al. 2021), while it is very close to the constrained region for δ Scuti stars on the CMD given by Gaia Collaboration et al. (2019). Therefore, we classified star 2483 as a δ Scuti variable. This star is an interesting target for further follow-up spectroscopic studies as it seems to be a binary star with a δ Scuti component.

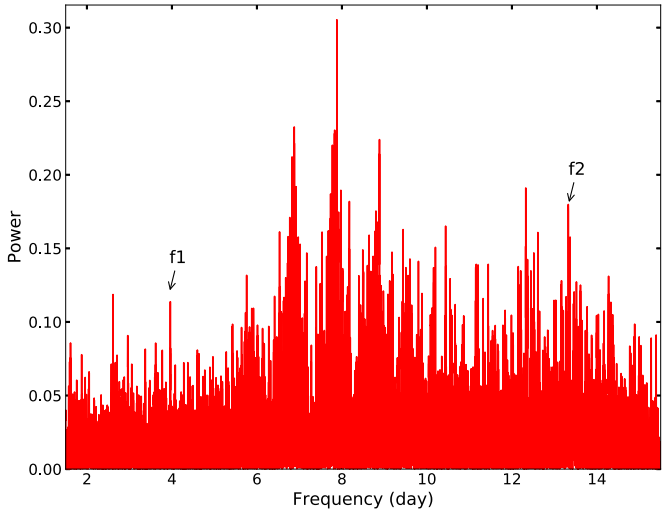

Figure 9. Power spectrum of star 2483. $f1$ denotes the frequency of the binary system while frequency $f2$ corresponds to δ Scuti-type variability.

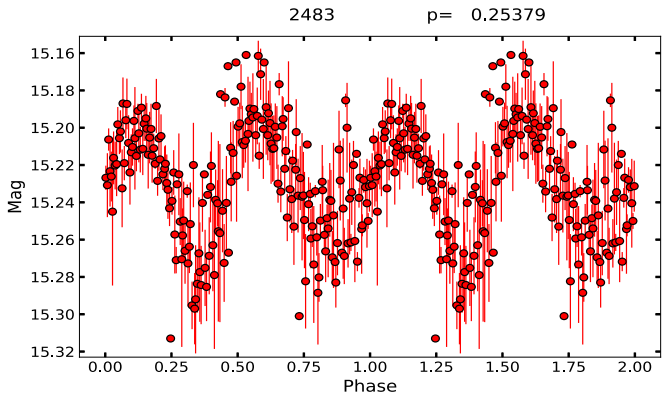

Figure 10. Plot illustrating the eclipsing nature of the δ Scuti star 2483. The light curve is constructed for the period of 0.25379 days.

5.3.2. γ Dor Variable Stars

γ Dor stars are g-mode pulsating stars with spectral class A7–F5 and lie in the γ Doradus instability strip in the H-R diagram. The location of the γ Dor variables on the H-R diagram is important for understanding the interior of stars as it is the transition zone where energy transfer changes from convective cores and radiative envelopes to radiative cores and convective envelopes. This property associated with γ Dor stars helps in constraining the theoretical models of heat transfer in stars. The pulsation in γ Dor stars is nonradial g-modes and the pulsation periods of these stars are between 0.3 and 3.0 days. The typical amplitude of variation for γ Dor stars is ∼0.1 mag. These stars are less massive than δ Scuti stars and range in mass from 1.5 $M_{\odot}$ to 1.8 $M_{\odot}$. The variable star with ID 1596 in our list of variables exhibits properties of a γ Dor star as suggested by its amplitude, period, and location in the γ Doradus instability strip. The location of this star on the CMD was in the region mostly occupied by γ Dor stars. Its period was found to be 0.43500 days. The effective temperature of star 1596 was 6739 K as reported by Anders et al. (2019), which is in the range 6700–7400 K expected for γ Dor stars. Therefore, we

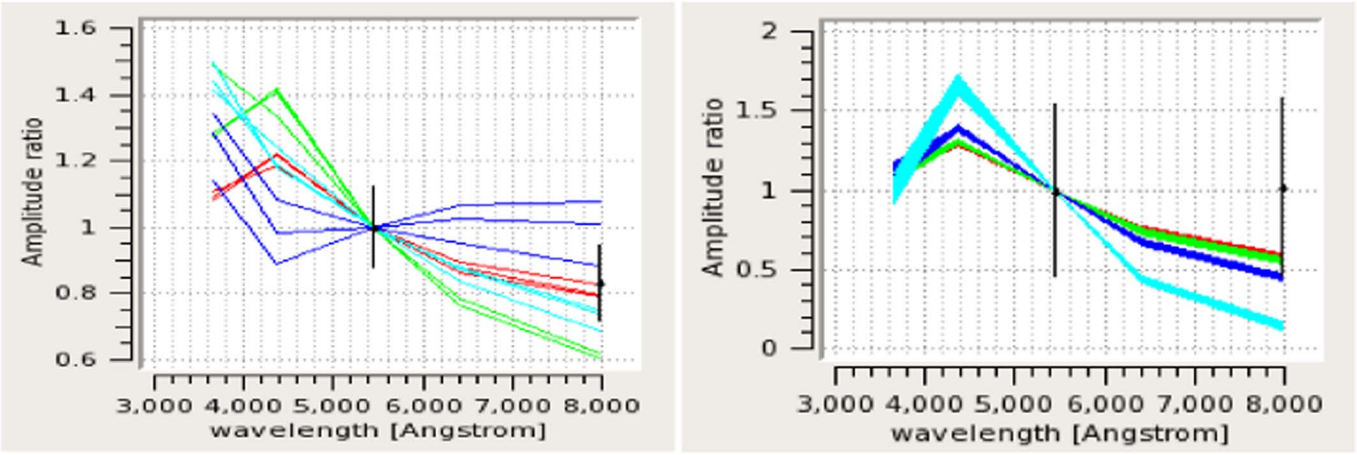

Figure 11. Plots of amplitude ratios for mode identification through the FAMIAS package using multiband photometric data. The left and right panels show plots of the amplitude ratios for stars 2483 and 1596, respectively. Modes $l = 0$, 1, 2, and 3 are shown by red, green, blue, and cyan respectively.

classified star 1596 as a γ Dor star. The pulsation mode of this γ Dor star was identified using multiband photometric data through FAMIAS software (Zima 2008) as discussed in the following section.

5.3.3. Mode Identification of Pulsation

We used time-series data obtained in V and I bands for the identification of the pulsation modes of δ Scuti and γ Dor stars through FAMIAS software packages (Zima 2008). The results are compared with prediction of models for $l = 0$, 1, 2, 3, and 4. The effective temperatures, surface gravity, and metallicity values required for model fitting in FAMIAS were taken from Anders et al. (2019). The multiband photometric mode determination using FAMIAS is based on the relation between amplitude ratios and phase differences obtained for various photometric bands (Watson 1988). We identified 2483 as a δ Scuti star while 1596 was characterized as a γ Dor star. Plots of amplitude ratios versus phase differences are given in Figure 11 for both the pulsating stars. The δ Scuti star 2483 was found to be pulsating in $l = 0$, which corresponds to radial pulsation (Ziaali et al. 2019; Jayasinghe et al. 2020b). We could not find a good fitting for star 1596, but it seems to be pulsating in $l = 0$ mode. The low harmonic degree of pulsation $l = 0$ is typical for δ Scuti and γ Dor stars (Sánchez Arias et al. 2017).

5.4. Misc Variables

Variable stars that could not be classified in any one type of variability class were called miscellaneous type. A total of 30 variable stars were classified as miscellaneous in the present study. Stars 2472, 2673, and 5451 lie between SPB and δ Scuti instability strips. This region in the H-R diagram is prohibited for pulsation according to standard stellar models. Mowlavi et al. (2016) classified these stars as fast-rotating pulsating B (FaRPB) variable stars based on a spectroscopic study that revealed that the majority of these stars were fast-rotating. FaRPB stars are known to have short periods ($p < 0.55$ days; Mowlavi et al. 2016; Joshi et al. 2020a). However, these variables were classified as miscellaneous variables since they have periods significantly longer than 0.55 days. The light curves of stars 1689 and 1935 show a hint of eclipsing binary but we could not confirm their exact nature and assigned the Misc category to them. Star 2245 was located near the blue edge of the δ Scuti instability strip. However, its period of 0.96225 days was significantly longer than the period of less than 0.3 days expected for δ Scuti stars. Star 737 lies close to the blue edge of the δ Scuti instability strip, but it has a period of 5.908 days, which is very high for any δ Scuti star.

The stars 1602 and 4049 have been classified as RS CVn variables in the AAVSO International Variable Star Index (VSX) catalog (Watson et al. 2006). RS CVn variables are eclipsing binary systems with a primary star of spectral class F–G. These binary systems are known to have asymmetric light curves caused by chromospheric activity and rotation. The distortion in the light curves is thought to be caused by an uneven distribution of surface cool spots (Eaton & Hall 1979; Eaton & Henry 2007). RS CVn variables show spectral emission lines of Ca II H and K (Zhang & Gu 2008). The light curves of these stars are the results of spot modulation of the eclipses. The light curves of these two variable stars are shown in Figure 12. It is clear from the figure that they do not exhibit clear eclipses, so these stars could be rotational or noneclipsing binaries with large spots on one or both components. However, the effective temperatures of the stars 1602 and 4049 were reported to be 6922 and 7988 K by Bai et al. (2019), indicating that these systems are earlier than K spectral type, which is a potential spectral class for RS CVn stars (Chen et al. 2020). The locations of stars 1602 and 4049 on the CMD are compatible with their classification as RS CVn variables. RS CVn stars with larger ($G_{BP} - G_{RP}$) color values generally have greater absolute G magnitudes (Gaia Collaboration et al. 2019). This tendency is also found to be true in the case of RS CVn stars identified in the present study, as can be seen in Table 3. Considering all these properties of the stars 1602 and 4049 we classify them as Miscellaneous variables.

5.5. Comparison

We searched for variable stars identified by us in the previously available catalogs of variable stars. We found 11 out of 57 variable stars identified by us to be reported in the VSX catalog. There were also eight variable stars in common with the catalog of periodic variable stars provided by Chen et al. (2020) using the ZTF data. The periods and classifications of these stars are given in Table 6 for comparison. The periods determined in the zg and zr bands of ZTF were found to differ significantly in the catalog of Chen et al. (2020) for a few stars. There were twice as many data points observed in the zr band

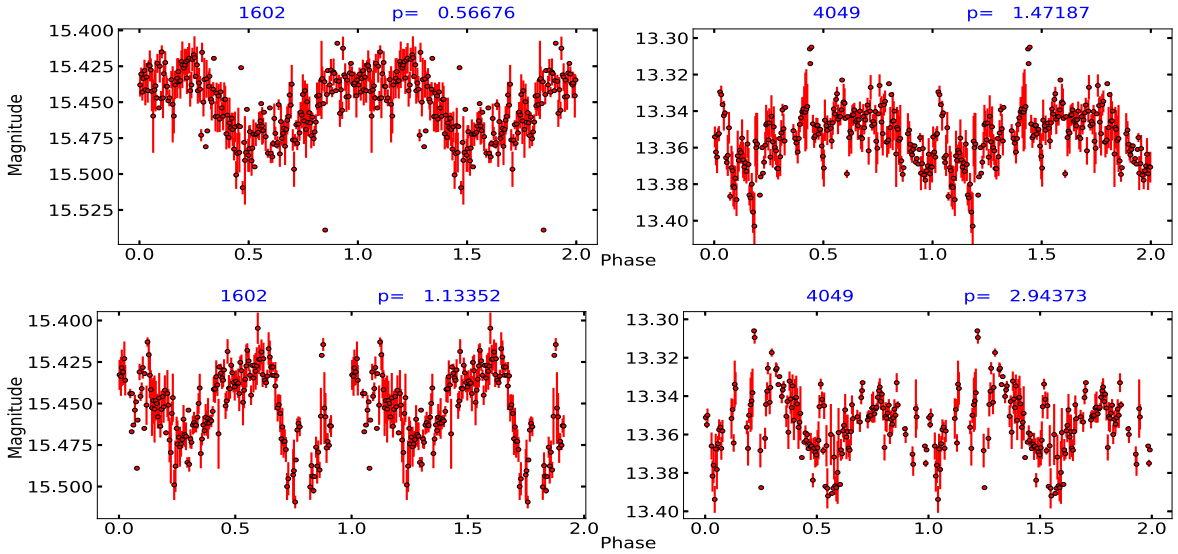

Figure 12. Possible RS CVn variable stars. The light curves in upper panel are for the obtained period while light curves in lower panel are plotted for twice the obtained period. The star IDs and periods are given on the top of each plot.

Table 6
Comparison of Periods and Variability Type of Variable Stars Reported in the VSX Catalog and the ZTF Catalog of Periodic Variable Stars Provided by Chen et al. (2020)

ID	$P_{\rm VSX}$ (day)	$\rm Type_{VSX}$	$P_{\rm ZTF}$ (day)	$\rm Type_{ZTF}$	P	Type
298	⋯	EA	8.54994	EA	2.88585	EA
732	0.30936	EW	⋯	⋯	0.30934	EW
1397	2.48934	EA/DM	⋯	⋯	2.48932	EA
1602	0.53806	RS CVn	0.53806	RS CVn	1.13352	Misc
1785	0.47660	EW	0.47660	EW	0.47661	EW
2458	0.27406	EW	0.27405	EW	0.27405	EW
2483	0.07504	δ Scuti	⋯	⋯	0.07504	δ Scuti
3005	0.31404	EW	0.31404	EW	0.31405	EW
3472	0.38883	EW	0.38883	EW	0.38882	EW
3535	0.31240	EW	0.32340	EW	0.32339	EW
4049	9.26598	RS CVn	9.26598	RS CVn	2.94373	Misc

Note. The periods and variability types determined by us are given in the last two columns.

as in the *zg* band for these eight stars, so we mention only periods in the *zr* band in Table 6. We found that the classifications of the variable stars given in these catalogs are generally in agreement with our classifications. We could not find evidence for the variables 1602 and 4049 to be RS CVn stars as they are reported in these catalogs. The periods given in the catalogs are mostly in agreement with the periods determined by us. The remaining 46 variables are not listed in any catalog of variable stars so they can be considered as new variable stars identified by us.

We also check the archive of the Transiting Exoplanet Survey Satellite (TESS) to compare our observations. We found six of our detected variable stars, namely 1397, 1596, 2302, 2472, 2673, and 4049, in TESS archives having simple aperture photometry (SAP) fluxes estimated using QLP pipelines. The cadence for these stars is 1800 s in the archived data. We could extract a very nice light curve for the star 1397, which is a bright star with TESS magnitude (Tmag) $\sim$ 9.7 mag (Paegert et al. 2021) showing periodicity of amplitude $\sim$0.3 mag (see Figure 13). The TESS data for stars 1596 and 2673 also produced good light curves, but the period for 2673 was different than ours. The time-series PSF fluxes of the stars 2999, 4361, and 5091 extracted using a PSF-based Approach to TESS High Quality Data of Stellar Clusters (PATHOS) pipeline were also available in the TESS archive. The light curve generated using TESS data for star 2999 was consistent with the period obtained from our observed data. We could not extract any signal of variability for the remaining five stars, probably due to the presence of systematic artifacts in SAP fluxes compared to presearch data conditioning SAP fluxes (Lin et al. 2019).

6. Summary and Conclusion

We extensively observed the open cluster region NGC 381 in V and I bands for the variability study. The region was observed using the 1.3 m DFOT telescope equipped with a 2k $\times$ 2k CCD having a large field of view of $\sim 18' \times 18'$ suitable for a variability search. The data were collected on 27 nights over a span of more than one year from 2017 October 1 to 2019 January 14. The data were reduced using the PSF technique and standard magnitudes were obtained. In the present study, we identified a total of 57 periodic variable stars in the cluster region NGC 381. These variable stars were classified on the basis of the shape of the light curves, period, amplitude, and location on H-R diagrams. We found one δ Scuti star and one γ Dor star. The pulsation modes of these variable stars were examined through the FAMIAS package using Johnson V-band and Cousins I-band data and the δ Scuti star was found to be pulsating in possibly the first overtone mode. To detect eclipsing binaries, we checked the light curves of all the periodic variables for twice the period obtained. The stars were qualified as eclipsing binaries only after distinct identification of primary and secondary minima. In this way we found a total of 10 eclipsing binaries comprising two eclipsing binaries of Algol type and eight of W UMa type. The physical parameters of the EW-type binaries were estimated using empirical relations and PHOEBE model fitting packages. We classified late-type variables as rotational variables if the color $(B-V)_0$ was found to be larger than 0.5 mag. We identified a total of 15 rotational variables in the present study. The

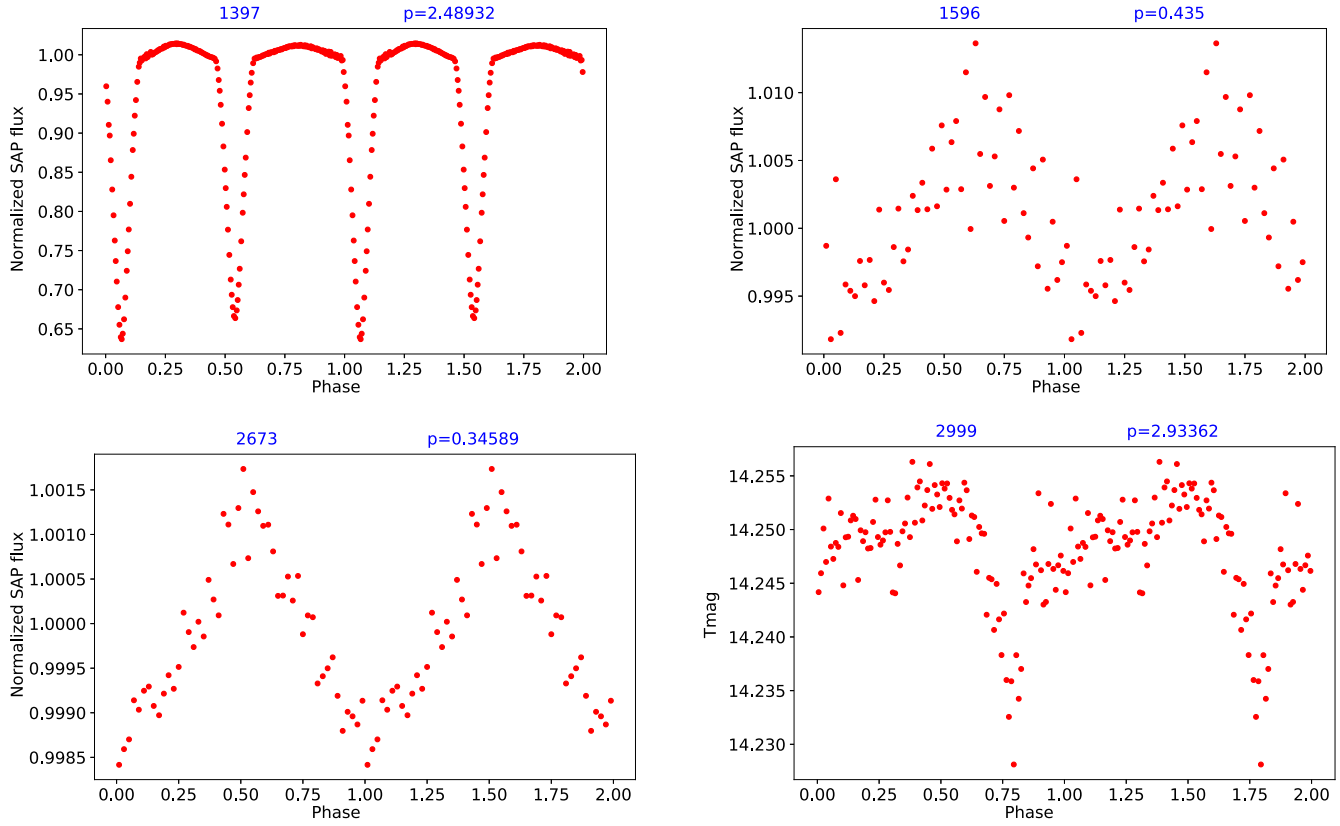

Figure 13. Light curves for variable stars found in TESS archives. The star IDs and periods are noted at the top of each plot. The TESS mag (Tmag) for the star ID 2999 is calculated from the PSF flux provided in the TESS archives using the relations given by Handberg et al. (2021).

rotational variability is thought to be present due to the uneven distribution of magnetic cool spots on the surface of the stars. There were also some variables that could not be classified as any particular type of variable and we classified them as miscellaneous type. A total of 30 variables were put in this class. However, more time-series data complemented with spectroscopic studies are necessary to characterize these variables.

This work presents results from the European Space Agency (ESA) space mission Gaia. Gaia data are being processed by the Gaia Data Processing and Analysis Consortium (DPAC). Funding for the DPAC is provided by national institutions, in particular the institutions participating in the Gaia MultiLateral Agreement (MLA). The Gaia mission website is https://www.cosmos.esa.int/gaia. The Gaia archive website is https://archives.esac.esa.int/gaia. This paper includes data collected by the TESS mission, which are publicly available from the Mikulski Archive for Space Telescopes (MAST) at the Space Telescope Science Institute (STScI). Funding for the TESS mission is provided by the NASA Explorer Program. STScI is operated by the Association of Universities for Research in Astronomy, Inc., under NASA contract NAS 5–26555. This research is also based on observations obtained with the Samuel Oschin Telescope 48 inch and the 60 inch telescope at the Palomar Observatory as part of the Zwicky Transient Facility project. The ZTF is supported by the National Science Foundation under grant No. AST-1440341 and a collaboration including Caltech, IPAC, the Weizmann Institute for Science, the Oskar Klein Center at Stockholm University, the University of Maryland, the University of Washington, Deutsches Elektronen-Synchrotron and Humboldt University, Los Alamos National Laboratories, the TANGO Consortium of Taiwan, the University of Wisconsin at Milwaukee, and Lawrence Berkeley National Laboratories. Operations are conducted by the COO, IPAC, and UW.

Software: IRAF (Tody 1986, 1993), DAOPHOT II (Stetson et al. 1990), PHOEBE (Prša & Zwitter 2005), FAMIAS (Zima 2008).

Appendix

The plots shown in Figure 14 of this section supplements the lightcurves of the 45 variable stars provided in Figure 3.

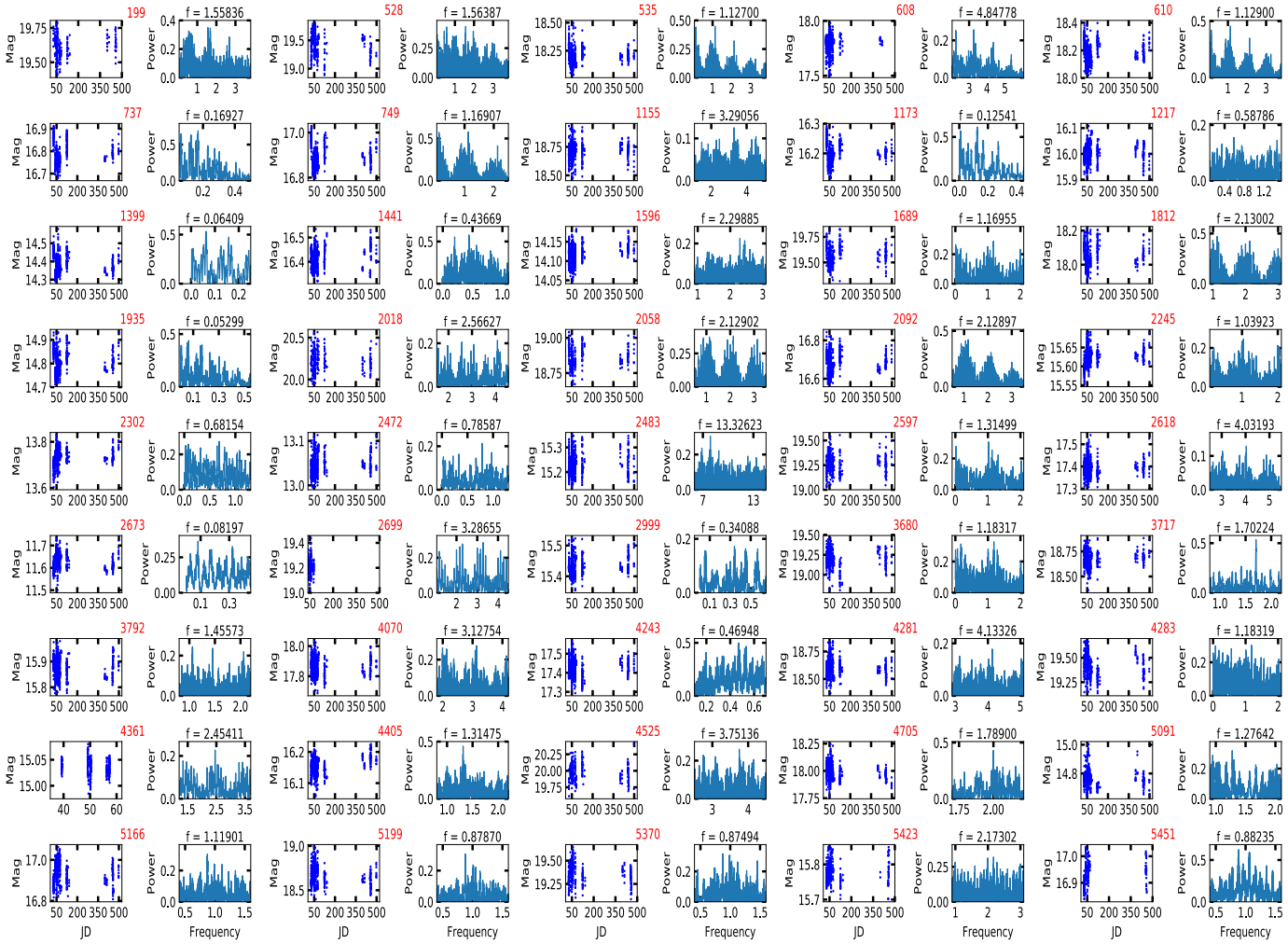

Figure 14. Plots of magnitude vs. Julian date and Lomb–Scargle periodogram for the 45 variable stars whose phase-folded light curves are shown in Figure 3. The star IDs and phase-folding frequencies are given at the top of each subplot.

ORCID iDs

Jayanand Maurya https://orcid.org/0000-0001-5119-8983
Y. C. Joshi https://orcid.org/0000-0001-8657-1573

References

Akeson, R. L., Chen, X., Ciardi, D., et al. 2013, PASP, 125, 989
Anders, F., Khalatyan, A., Chiappini, C., et al. 2019, A&A, 628, A94
Angus, R., Morton, T. D., Foreman-Mackey, D., et al. 2019, AJ, 158, 173
Arentoft, T., Bouzid, M. Y., Sterken, C., Freyhammer, L. M., & Frandsen, S. 2005, PASP, 117, 601
Bai, Y., Liu, J., Bai, Z., Wang, S., & Fan, D. 2019, AJ, 158, 93
Bailer-Jones, C. A. L., Rybizki, J., Fouesneau, M., Mantelet, G., & Andrae, R. 2018, AJ, 156, 58
Balona, L. A., Pigulski, A., De Cat, P., et al. 2011, MNRAS, 413, 2403
Barnes, S. A. 2007, ApJ, 669, 1167
Bedding, T. R., Murphy, S. J., Hey, D. R., et al. 2020, Natur, 581, 147
Bellm, E. C., Kulkarni, S. R., Graham, M. J., et al. 2019, PASP, 131, 018002
Breger, M. 2000, in ASP Conf. Ser. 210, Delta Scuti and Related Stars, ed. M. Breger & M. Montgomery (San Francisco, CA: ASP), 3
Cantat-Gaudin, T., Jordi, C., Vallenari, A., et al. 2018, A&A, 618, A93
Chen, X., Wang, S., Deng, L., et al. 2020, ApJS, 249, 18
Ciardi, D. R., von Braun, K., Bryden, G., et al. 2011, AJ, 141, 108
Drake, A. J. 2006, AJ, 131, 1044
Drake, A. J., Djorgovski, S. G., Catelan, M., et al. 2017, MNRAS, 469, 3688
Eaton, J. A., & Hall, D. S. 1979, ApJ, 227, 907
Eaton, J. A., & Henry, G. W. 2007, PASP, 119, 259
Gaia Collaboration, Eyer, L., Rimoldini, L., et al. 2019, A&A, 623, A110
Gazeas, K. D. 2009, CoAst, 159, 129
Green, G. M., Schlafly, E., Zucker, C., Speagle, J. S., & Finkbeiner, D. 2019, ApJ, 887, 93
Hambálek, Ľ., & Pribulla, T. 2013, CoSka, 43, 27
Handberg, R., Lund, M. N., White, T. R., et al. 2021, AJ, 162, 170
Hwang, H.-C., & Zakamska, N. L. 2020, MNRAS, 493, 2271
Iorio, G., & Belokurov, V. 2019, MNRAS, 482, 3868
Jayasinghe, T., Stanek, K. Z., Kochanek, C. S., et al. 2020a, MNRAS, 493, 4045
Jayasinghe, T., Stanek, K. Z., Kochanek, C. S., et al. 2020b, MNRAS, 493, 4186
Jiang, D. 2020, MNRAS, 492, 2731
Jiang, D., Han, Z., & Li, L. 2014, MNRAS, 438, 859
Joshi, Y. C., Jagirdar, R., & Joshi, S. 2016, RAA, 16, 63
Joshi, Y. C., John, A. A., Maurya, J., et al. 2020a, MNRAS, 499, 618
Joshi, Y. C., Maurya, J., John, A. A., et al. 2020b, MNRAS, 492, 3602
Latković, O., Čeki, A., & Lazarević, S. 2021, ApJS, 254, 10
Liakos, A., & Niarchos, P. 2017, MNRAS, 465, 1181
Lin, C. L., Ip, W. H., Hou, W. C., Huang, L. C., & Chang, H. Y. 2019, ApJ, 873, 97
Lomb, N. R. 1976, Ap&SS, 39, 447
Long, L., Zhang, L.-y., Bi, S.-L., et al. 2021, ApJS, 253, 51
Mamajek, E. E., & Hillenbrand, L. A. 2008, ApJ, 687, 1264
Maurya, J., & Joshi, Y. C. 2020, MNRAS, 494, 4713
Minniti, J. H., Sbordone, L., Rojas-Arriagada, A., et al. 2020, A&A, 640, A92
Miszuda, A., Szewczuk, W., & Daszyńska-Daszkiewicz, J. 2021, MNRAS, 505, 3206
Mowlavi, N., Saesen, S., Semaan, T., et al. 2016, A&A, 595, L1
Norton, A. J., Payne, S. G., Evans, T., et al. 2011, A&A, 528, A90
Paegert, M., Stassun, K. G., Collins, K. A., et al. 2021, arXiv:2108.04778

Panchal, A., & Joshi, Y. C. 2021, AJ, 161, 221
Pietrzyński, G., Graczyk, D., Gallenne, A., et al. 2019, Natur, 567, 200
Prša, A., & Zwitter, T. 2005, ApJ, 628, 426
Qian, S. B., Zhang, J., He, J. J., et al. 2018, ApJS, 235, 5
Rucinski, S. M. 2007, MNRAS, 382, 393
Sánchez Arias, J. P., Córsico, A. H., & Althaus, L. G. 2017, A&A, 597, A29
Sandquist, E. L., Stello, D., Arentoft, T., et al. 2020, AJ, 159, 96
Sanghi, A., Vanderbosch, Z. P., & Montgomery, M. H. 2021, AJ, 162, 133
Scargle, J. D. 1982, ApJ, 263, 835
Skowron, D. M., Skowron, J., Mróz, P., et al. 2019, Sci, 365, 478
Skumanich, A. 1972, ApJ, 171, 565
Soares-Furtado, M., Hartman, J. D., Bhatti, W., et al. 2020, ApJS, 246, 15
Stassun, K. G., & Torres, G. 2021, ApJL, 907, L33
Stetson, P. B. 1987, PASP, 99, 191
Stetson, P. B., Davis, L. E., & Crabtree, D. R. 1990, in ASP Conf. Ser. 8, CCDs in Astronomy, ed. G. H. Jacoby (San Francisco, CA: ASP), 289
Tody, D. 1986, Proc. SPIE, 627, 733
Tody, D. 1993, in ASP Conf. Ser. 52, Astronomical Data Analysis Software and Systems II, ed. R. J. Hanisch, R. J. V. Brissenden, & J. Barnes (San Francisco, CA: ASP), 173
Torres, G. 2010, AJ, 140, 1158
Torres, G., Andersen, J., & Giménez, A. 2010, A&ARv, 18, 67
Uytterhoeven, K., Moya, A., Grigahcène, A., et al. 2011, A&A, 534, A125
van Saders, J. L., & Pinsonneault, M. H. 2013, ApJ, 776, 67
Wang, S., & Chen, X. 2019, ApJ, 877, 116
Watson, C. L., Henden, A. A., & Price, A. 2006, SASS, 25, 47
Watson, R. D. 1988, Ap&SS, 140, 255
Xue, H.-F., Fu, J.-N., Mowlavi, N., et al. 2019, MNRAS, 482, 658
Yildiz, M., & Doğan, T. 2013, MNRAS, 430, 2029
Zhang, L. Y., & Gu, S. H. 2008, A&A, 487, 709
Ziaali, E., Bedding, T. R., Murphy, S. J., Van Reeth, T., & Hey, D. R. 2019, MNRAS, 486, 4348
Zima, W. 2008, CoAst, 157, 387